Polarization-Modulated Second Harmonic Generation Ellipsometric Microscopy at Video Rate

Emma L. DeWalt, Shane Z. Sullivan, Paul D. Schmitt, Ryan D. Muir, and Garth J. Simpson*

Department of Chemistry, Purdue University, 560 Oval Drive, West Lafayette, Indiana 47907, United States

W *Web-Enhanced Feature* **S** *Supporting Information*

ABSTRACT: Fast 8 MHz polarization modulation coupled with analytical modeling, fast beam-scanning, and synchronous digitization (SD) have enabled simultaneous nonlinear optical Stokes ellipsometry (NOSE) and polarized laser transmittance imaging with image acquisition rates up to video rate. In contrast to polarimetry, in which the polarization state of the exiting beam is recorded, NOSE enables recovery of the complex-valued Jones tensor of the sample that describes all polarization-dependent observables of the measurement. Every video-rate scan produces a set of 30 images (10 for each detector with three detectors operating in parallel), each of which corresponds to a different polarization-dependent result. Linear fitting of this image set contracts it down to a set of five parameters for each detector in second harmonic generation (SHG) and three parameters for the transmittance of the incident beam. These parameters can in turn be used to recover the Jones tensor elements of the sample. Following validation of the approach using z-cut quartz, NOSE microscopy was performed for microcrystals of both naproxen and glucose isomerase. When weighted by the measurement time, NOSE microscopy was found to provide a substantial (>7 decades) improvement in the signal-to-noise ratio relative to our previous measurements based on the rotation of optical elements and a 3-fold improvement relative to previous single-point NOSE approaches.
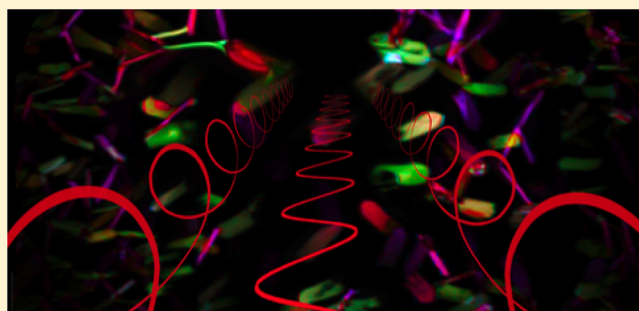
INTRODUCTION

Polarization-dependent optical microscopy can provide rich information on local structure and orientation, with the benefits particularly pronounced in nonlinear optics (NLO) by nature of the greater number of photons involved in the light−matter interactions. In the case of second harmonic generation (SHG), up to six independent parameters can be recovered from a single measurement, whereas only two are typically accessible in linear optics. In biological samples, polarization-dependent SHG microscopy has been used to great effect in the analysis of collagen,[1−3] cell membranes,[4] and other ordered biological motifs,[5,6] and has been extended to in vivo studies of cancer, musculoskeletal disorders, cardiovascular disease, and corneal disorders.[5−9] Polarization-dependent SHG imaging has also been used for inorganic materials characterization,[10−12] crystal domain imaging,[13] and surface analysis.[14,15]

Despite these successes, the most common approaches for polarization imaging are based on rotation of waveplates/polarizers, which suffer from some significant limitations. First, mechanical methods of polarization modulation are typically relatively slow, introducing significant $1/f$ noise into the measurement. In addition, the sample can change over time from sample motion, which represents a challenge particularly for in vivo imaging. Bleaching and/or thermal effects induced by laser exposure can also result in systematic bias and increased uncertainty in the parameters extracted from the polarization dependence.

Numerous strategies have been taken to reduce the time frame for polarization analysis in SHG microscopy to address these limitations. In exceptional early studies by Stoller et al.,[2] polarization modulation at 4 kHz was performed in sample-scanning microscopy measurements of rat tail tendon. Detection of the modulation harmonics was performed using two lock-in amplifiers per detector. Tanaka et al.[16] have included fast polarization modulation using an electro-optic modulator (EOM) toggling between two fixed polarization states on a per-pixel basis. Lien et al.[17] have performed polarization modulation for SHG imaging using a liquid crystal modulator, which had a response time on the order of several milliseconds. With the exception of the work by Tanaka et al., these techniques have only been demonstrated at relatively low frame rates (several seconds to hours per frame). Furthermore, none of the techniques directly recover the $\chi^{(2)}$ tensor elements driving the nonlinear response of the sample, which is a key step in quantitative modeling to predictively connect local structure to the observed response.

In the present study, quantitative polarization analysis in SHG microscopy is demonstrated based on nonlinear optical Stokes ellipsometry (NOSE). This effort builds on previous work, in which NOSE has been shown to provide a substantial (7
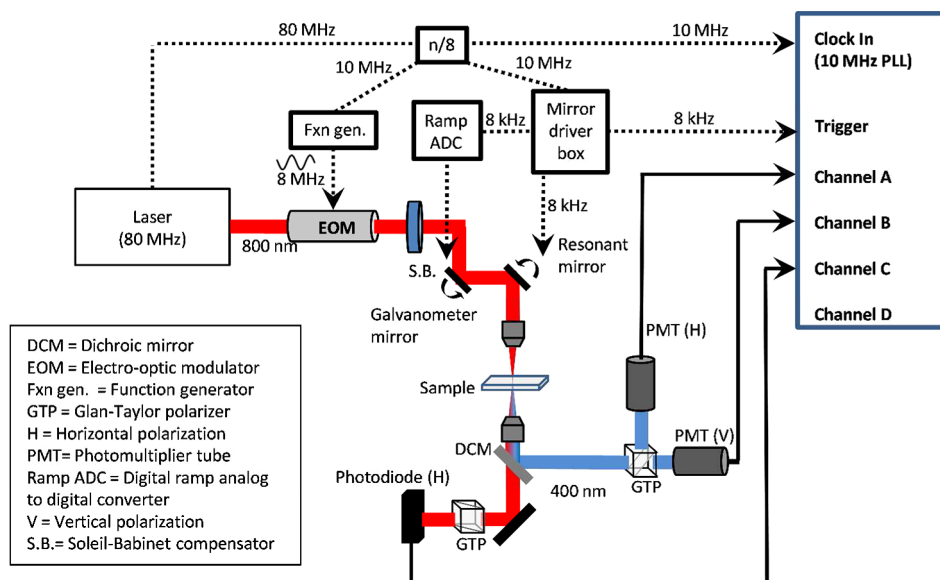
Figure 1. Instrument and timing schematic for a SHG and laser transmittance microscope capable of synchronous polarization modulation. The master clock for controlling the scanning mirrors and for data acquisition is provided by the laser, originally an 80 MHz signal, divided by 8 to generate a 10 MHz clock.

decade) improvement in the signal-to-noise of polarization-dependent SHG measurements compared to approaches based on the physical rotation of optical elements.[14,18] This advantage was found to arise primarily through reduction of $1/f$ noise from slow changes in the source, detector, and sample over the time-course of the polarization measurement. However, previous implementations of NOSE required practical analysis times of several milliseconds per pixel,[14,18] which is a prohibitively lengthy measurement time per-pixel for reasonable imaging applications. By combining high speed (8 MHz) polarization modulation using an EOM with synchronous digitization (SD), the time frame for NOSE was reduced to as low as 150 ns per pixel, enabling full polarization analysis at each pixel at up to video-rate frame rates. Under an applied sinusoidal voltage, the EOM imparts time-varying phase shifts between the horizontal and vertical components of light that pass through it, producing a series of elliptical polarizations for the exiting beam. In the present study, 10 polarization states were sampled with each period of the EOM and three simultaneous channels of data were acquired, resulting in a set of 30 raw polarization-dependent images produced for each frame. A total of 5 independent observables in SHG per detector and 3 observables in laser transmittance are experimentally allowed, corresponding to 13 unique degrees of freedom recovered at each pixel in each frame at video rate.

The ability of this method to be performed at up to video rate is expected to reduce artifacts from sample movement, improving compatibility with in vivo measurements from structural features of collagen in living specimens. In addition, the sensitivity and speed of video rate NOSE measurements should also provide a method of rapid polymorph screening for active pharmaceutical ingredient (API) crystals, where different polymorphs will generally exhibit different polarization-dependent NLO responses. Although the primary goal of the present work is to describe the methodology, instrumentation and validation of video rate NOSE imaging for recovering model-independent observables, the aforementioned applications will be the subjects of future studies.

■ EXPERIMENTAL METHODS

Instrumentation. SHG and laser transmittance measurements were performed on a custom microscope adapted from an instrument described previously[12,19,20] and shown schematically in Figure 1. Briefly, an 80 MHz 100 fs MaiTai Ti:sapphire laser (SpectraPhysics) tuned to 800 nm was used as the incident light source for both SHG and laser transmittance imaging, with average powers between 20 and 220 mW. The beam was scanned across the sample using a resonant scanning mirror at 8 kHz (EOPC) synchronized to the laser and a galvanometer mirror (CambridgeTech) in the fast and slow axes, respectively. The beam was passed through an EOM rotated 45° from its fast-axis. A Soleil-Babinet compensator was placed after the EOM to correct for polarization changes induced by the rest of the beam path and microscope components. The beam was then directed through a telecentric lens pair and square aperture to block the turning points of the sinusoidal resonant mirror trajectory. The scanned beam was focused onto the sample with a 10×, 0.3 NA objective (Nikon). SHG and fundamental light were separated using a dichroic mirror and collected in the transmitted direction. The SHG signal was separated into its horizontal and vertical components with a Glan-Taylor polarizer, which were detected on two photomultiplier tubes (PMTs) (Hamamatsu H12310-40) with bandpass filters (HQ 400/20m-2p; Chroma Technology) to further reject the fundamental. The transmitted fundamental light was detected with a photodiode (Thorlabs DET-10A) after passing through a Glan-Talyor polarizer set to pass horizontal, allowing for simultaneous polarized laser transmittance imaging and SHG imaging.

Data Acquisition. Data acquisition was performed using SD.[20] A schematic of the synchronous timing control required for SD is depicted in Figure 1. Two PCIe digitizer cards (AlazarTech ATS-9350) were used to flash digitize the SHG and laser transmittance on three channels synchronously with the laser. Custom software was designed to record digitized voltages as 32-bit numbers. The 80 MHz signal from the laser's internal photodiode was used as the master clock. The laser clock was sent through a custom timing module, where it was amplified,

shifted, and divided by 8, to produce a 10 MHz square wave. The synchronous 10 MHz signal was sent to the onboard 10 MHz phase-locked-loop of the digitizer card, and the digitizer card was set to digitize at 80 MHz synchronously with the laser.

Due to the high Q-factor of the resonant mirrors ($Q > 250$) amplitude stability was achieved at the sacrifice of phase stability. To correct for this drift in phase stability, a custom control box was designed and built to perform real-time active phase correction of the resonant mirror. The resonant mirror timing box was controlled by an 8-bit microcontroller (Silicon Laboratories, C8051f120), running at 80 MHz derived from an external 10 MHz phase-lock loop (PLL) synchronous with the 80 MHz master clock from the Ti:sapphire laser, allowing for precise knowledge of the number of laser pulses per resonant mirror trajectory. The microcontroller ran a custom built operating system using a combination of hardware and software timers to produce the mirror drive signal. The feedback of the resonant mirror was analyzed by the box, and corrections to the driving phase were made to maintain phase stability of the resonant mirror. Phase corrections were performed to a precision of 25 ns, or two clock ticks from the master clock. A monitor output signal from the mirror driver box was sent to the trigger input on the digitizer card. A synchronous ramp signal generated by the timing module was used to control the galvanometer mirror by incrementing the angle of the mirror after every pass of the resonant mirror.

The signal transients from each individual detector response from every laser pulse were digitized synchronously with the laser. A 3−13 ns electronic digital delay stage was added between the master clock (10 MHz) signal and the PCIe digitizer cards to allow for adjustment of the phase of digitization relative to the signal generation to account for the absolute time difference of the clock and the optical path. The resultant data were then binned following a sine-wave trajectory, resulting in higher density of sampling near the turning points of the trajectory (Figure S-1 in the Supporting Information), with the corresponding data analysis accounting for this sampling density.

Polarization Modulation. Synchronous polarization modulation was performed using a custom-built extended length EOM (Conoptics). A third 10 MHz output from the timing module was used as an external clock source for a function generator, which was used to generate an 8 MHz sine wave. The 8 MHz signal was amplified using a high voltage amplifier (AR Worldwide KAW1040) combined with a custom built resonant tank circuit and used to drive the EOM beyond its half-wave voltage. The period of the resonant mirror was carefully chosen using its driver box, so that the number of laser pulses per image was an integer multiplier of the number of polarizations used to ensure that each frame began with the same starting polarization. For the described experiments, the laser frequency was 80 MHz and the EOM was driven at 8 MHz for a total of 10 unique elliptical polarizations. Custom software (Matlab) was developed to separate out each laser pulse to generate the 10 polarization-dependent images in real-time. To ensure all 10 polarizations were sampled in one trajectory of the resonant mirror, pixels were binned in the fast-axis to generate images that were 300 by 512 pixels. After acquisition, images were resized to 512 by 512 pixels using image interpolation (ImageJ).

Sample Preparation and Imaging. Polarization-dependent imaging was performed on z-cut quartz (500 μm thickness) at various rotation angles about the z-axis. Images of z-cut quartz were acquired with 20 mW average power and signal averaged

for ~2 s. Polarization-dependent imaging was performed on naproxen recrystallized in isopropanol with 95 mW average power. Video rate imaging was performed to generate polarization-dependent movies of the sample being translated using an automated sample stage (Prior). Still images of naproxen crystals indexed matched in Type A immersion oil were acquired with 64 frames averaged. Glucose isomerase was obtained as a crystalline suspension, and was dialyzed against 10 mM HEPES, 1 mM $MgCl_2$ and 100 mM HEPES, 10 mM $MgCl_2$. The protein solution was concentrated to 26 mg/mL in water and crystallized in 0.7 M sodium citrate tribasic dihydrate at pH 7 in a 96-well sitting drop crystallization tray (Corning). Polarization-dependent imaging of glucose isomerase crystals was performed in situ with 225 mW average power. Photon counting was performed with data acquisition times of ~2 min. Images were acquired in 3D through the drop using automated focus control (Prior) with 15 μm steps in the z-direction.

■ THEORETICAL FOUNDATION

Nonlinear optical ellipsometry is defined to be the determination of the relative Jones tensor elements describing the nonlinear optical response of the sample.[21,22] This definition is directly analogous to conventional linear ellipsometry for thin film analysis, in which the relative values of the diagonal elements in the Jones matrix describing surface reflection (typically) are determined experimentally.[23] NOSE is one specific method to perform nonlinear optical ellipsometry based on Stokes polarimetry, in which the polarization state of the exiting nonlinear beam is determined from the combined intensities measured by several detectors, each probing different polarization-dependent responses.[14,18]

The relationship between the detected intensity and a modulated incident polarization state in NOSE has been described in detail in previous works[14,18,24] and is only briefly summarized herein. In linear optics, the incident polarization state can be described in terms of well-established Jones vectors and Jones matrices. Recently, this framework has been extended to introduce the concept of Jones tensors as polarization transfer tensors.[22,25] By analogy with Jones matrices, knowledge of the Jones tensor allows one to predict all polarization-dependent observables of a given measurement as a function of the incident polarization state or states. In this framework, the Jones matrix for the EOM rotated an angle γ is given by the following expression.

$$M_{\text{EOM}}(t) = R(-\gamma)\begin{pmatrix} e^{i\Delta(t)/2} & 0 \\ 0 & e^{-i\Delta(t)/2} \end{pmatrix} R(\gamma) \tag{1}$$

The time-dependent phase shift of the EOM, $\Delta(t)$, is in turn sinusoidally modulated.

$$\Delta(t) = A\sin(2\pi f_0 t + \delta) + B \tag{2}$$

In eq 2, A represents the amplitude of modulation, f_0 is the modulation frequency in cycles/s, δ is the phase shift between the driving sinusoidal function and the experimental phase of the EOM, and B is the constant residual phase shift inherent in the EOM.

We have previously derived expressions relating the Jones tensor elements to the intensity of n-polarized SHG where n is either v or h for vertical or horizontal polarization, respectively.[14,18,24]

$$I_{det}^{2\omega} \propto A \cos^4\left(\frac{\Delta}{2}\right) + B \cos^3\left(\frac{\Delta}{2}\right)\sin\left(\frac{\Delta}{2}\right)$$
$$+ C \cos^2\left(\frac{\Delta}{2}\right)\sin^2\left(\frac{\Delta}{2}\right) + D \cos\left(\frac{\Delta}{2}\right)\sin^3\left(\frac{\Delta}{2}\right)$$
$$+ E \sin^4\left(\frac{\Delta}{2}\right) \tag{3}$$

$$A_n = |\chi_{nhh}|^2$$
$$B_n = -4\mathrm{Im}[(\chi_{nhh})(\chi_{nvh})]$$
$$C_n = 4|\chi_{nvh}|^2 - 2\mathrm{Re}[(\chi_{nhh})(\chi_{nvv})^*]$$
$$D_n = 4\mathrm{Im}[(\chi_{nvv})(\chi_{nvh})]$$
$$E_n = |\chi_{nvv}|^2 \tag{4}$$

In the above equation, the χ-terms indicate individual elements from the $2 \times 2 \times 2$ $\chi^{(2)}$ Jones tensor. From this above equation, it is clear that the measured intensity can generally recover up to five unique parameters ultimately dependent on three nonzero tensor elements, which in general are complex-valued. Since the number of real and imaginary unknowns exceeds the number of observables by one, only the relative phase between the tensor elements can be recovered, which is similar to conventional ellipsometry performed for surface analysis. Far from resonance and in the absence of birefringence in the sample, B and D are zero-valued, reducing the number of observables down to three, paired to the number of unique elements within the Jones tensor for a given polarization state of detection.

In practice, it is often more convenient to perform the linear fitting to an alternative set of Fourier functions. Conversion from the polynomial to Fourier coefficients is performed through simple matrix multiplication. The use of Fourier coefficients also provides direct comparison with alternative measurements performed by lock-in detection.[2] In this framework, the detected intensity is described by the following analytical expression.

$$I_{det}^{2\omega}(\Delta) \propto a + b\cos(2\Delta) + c\cos(\Delta) + d\sin(\Delta)$$
$$+ e\sin(2\Delta) \tag{5}$$

Interconversion between the two sets of coefficients can be achieved by simple matrix multiplication.

$$\begin{bmatrix} A \\ B \\ C \\ D \\ E \end{bmatrix} = \begin{bmatrix} 1 & 1 & 1 & 0 & 0 \\ 0 & 0 & 0 & 2 & 4 \\ 2 & -6 & 0 & 0 & 0 \\ 0 & 0 & 0 & 2 & -4 \\ 1 & 1 & -1 & 0 & 0 \end{bmatrix} \cdot \begin{bmatrix} a \\ b \\ c \\ d \\ e \end{bmatrix} \tag{6}$$

An analogous framework can be used to describe the polarization-dependent transmittance of the incident infrared beam, which in turn provides information on the sample birefringence, and is described in detail in the Supporting Information. In brief, the intensity of the transmitted beam under the conditions identical to those used for the SHG measurements is given by the following expression.

$$I_{det}^{\omega}(\Delta) \propto a + b\cos(\Delta) + c\sin(\Delta) \tag{7}$$

From eqs 5 and 7, it should be clear that the detected response will generally exhibit amplitude and phase terms for both the fundamental and second harmonic in Δ, in addition to a constant term. However, Δ is itself sinusoidally modulated in time. As a result, direct recovery of the Fourier coefficients from the Δ-dependent intensity is straightforward, but analogous quantitative analysis based on the harmonics of f_0 from the time-dependent intensity with sinusoidal modulation is not trivial. Previous early efforts have addressed this challenge by using sawtooth modulation that is linear in time.[2] However, this strategy is challenging to implement at high speeds because of the much larger bandwidth required to drive sawtooth modulation at MHz frequencies relative to sinusoidal modulation. In the present case, the use of a resonant tank circuit significantly increased the amplitude of modulation (which can be challenging at radio frequencies) and improved the stability through bandwidth reduction, but was fundamentally incompatible with sawtooth modulation.

The preceding treatments are valid within the paraxial approximation consistent with low numerical aperture lenses and objectives as used in the present study. However, it is relatively straightforward in principle to extend this mathematical framework for polarization analysis to high numerical aperture objectives in which the electric field has projections along all three spatial coordinates, as detailed explicitly in previous work.[22] In brief, the matrix-notation for propagation of the electric fields as presented in the present study allows the influence of tight focusing to be incorporated through multiplication by an additional "local field" matrix. This additional matrix relates the incoming and exiting local fields experienced within the focal volume to the far-field polarization state detected in the laboratory frame. Consequently, the present polarization modulation approaches can be easily extended to analogous measurements performed with high numerical aperture objectives.

■ RESULTS AND DISCUSSION

Quantitative analysis of the polarization-dependent nonlinear optical response was enabled first through characterization of the incident polarization state of the fundamental beam at each firing of the laser. Measurement of the transmitted polarized fundamental beam allowed for evaluation of the time-dependent phase angle of the EOM, which in turn defines the polarization state of the incident light. Polarized laser transmittance images are able to be obtained simultaneously with SHG images, allowing for characterization of the polarization state while the SHG images were acquired. An additional independent method was used to evaluate the phase angle of the EOM, through the detected second harmonic beam. Z-cut quartz has well-established relationships between the nonzero tensor elements dictated by symmetry, and exhibits no birefringence for light propagating parallel to the z-axis. The absence of birefringence minimizes the impact of polarization changes induced in either the incident fundamental or produced second harmonic beams that are not accounted for by the model. A nonlinear fit of experimental intensity to the theoretical intensity as a function EOM modulation (eqs 1 and 2) was performed for both polarized laser transmittance and horizontally polarized SHG. The results of both approaches are summarized in Figure 2 for representative data acquired with a quartz rotation angle of 30°.

Reasonably good agreement was achieved between the two techniques despite the substantial differences in the measured time-dependent intensities used in the fits, as shown in Figure 2c. Although a relatively subtle offset remains between the two calculated phase angles, the good overall agreement suggests
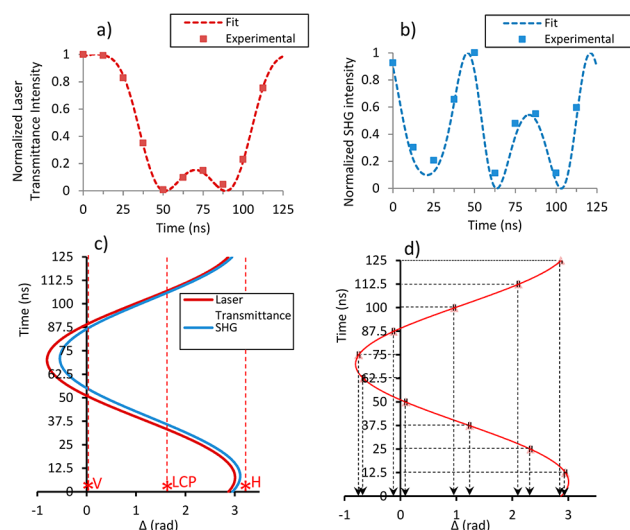
Figure 2. Nonlinear fitting of (a) horizontally polarized transmitted fundamental beam and (b) horizontally polarized SHG for z-cut quartz rotated to 30° and (c) the EOM phase, Δ, as determined from the two nonlinear fits. The Δ values for horizontal (H), vertical (V), and left-circularly polarizations are also indicated. The relationship of Δ as a function of time is demonstrated in (d) for nonlinear fitting of laser transmittance.

Figure 3. Linear fitting results of polarization-dependent SHG image stacks of z-cut quartz rotated at 30° for the horizontal PMT. Representative single-pixel fits are shown in (a) and (b), and a fit to the average response of 1×10^4 pixels is shown in (c).

that the incident polarization state can be reliably recovered from measurements of the polarized infrared beam. Uncertainties in the parameters A, δ, and B from eq 2 were determined through numerically calculating the second derivative around the minimum of chi-square space as described elsewhere, and propagated to determine the standard deviation in the phase values obtained from the fit.[26] The values derived from the nonlinear fit for A, δ, and B were 1.90 ± 0.04, 1.18 ± 0.02, and 1.10 ± 0.02, respectively, and the standard deviations for Δ are all $\sim \pm 0.04$.

Using the values for Δ recovered by the nonlinear fitting process for laser transmittance, the polarization-dependent SHG response was measured at multiple rotation angles of quartz. Linear fitting of the data to eq 5 was then performed was then performed to extract the Fourier coefficients. Figure 3 shows representative results for z-cut quartz, performing the linear fit on both a per-pixel basis (a, b) and across the average of 10^4 pixels (c). Derived Fourier coefficients across multiple rotation angles of z-cut quartz are summarized in Figure 4. Coefficients a and b are predicted by theory to be nonzero, with coefficients $c-e$ predicted to be zero. Coefficients $c-e$ extracted from the linear fitting of experimental data were centered about zero and are shown in Figure S-2 in the Supporting Information. Results reported in Figure 4 are for the average response over an area of 100×100 pixels. Images were integrated over 32 consecutive frames, corresponding to a minimum single pixel acquisition time of 4.8 μs. For comparison, the theoretical results are also included for the anticipated coefficients expected using the established nonlinear optical properties of quartz[27] and the measured Δ.

The recovered coefficients were in reasonably good agreement with those predicted by symmetry for z-cut quartz. Systematic departures were observed, increasing at quartz rotation angles approaching 30°. This departure is attributed to a combination of residual uncertainties in the phase angles (subtle errors can have significant effects), subtle residual birefringence in the quartz from imperfections in the cut, and
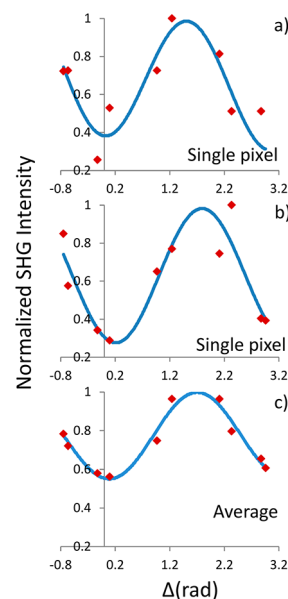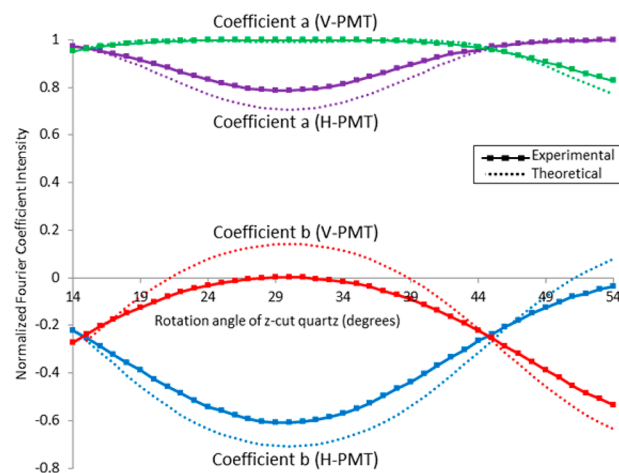

Figure 4. Experimental and theoretical normalized Fourier coefficients a and b for the vertical and horizontal SHG detectors as a function of rotation angle for z-cut quartz.

the breakdown of the assumption of plane polarized light after focusing through the objective. Although the SNR was lower in measurements obtained in 4.8 μs from single pixels, the recovered fits and resulting coefficient values were consistent between the single pixels and the entire field of view. For a given rotation of z-cut quartz, the five Fourier coefficients extracted from the linear fitting were converted to polynomial coefficients (eq 6) and subsequently converted into six Jones tensor elements (taking advantage of the interchangeability of the latter two subscripts in SHG), as described in the Supporting Information, eq S-6. This process was performed for seven rotation angles of z-cut quartz (15°, 20°, 25°, 30°, 35°, 40°, and 45°). The Jones tensors obtained for each of the seven known rotation angles were converted to the tensor for quartz rotated to 0° using eq S-4 in the Supporting Information, the results of which are summarized in Table 1.

Table 1. Experimental and Theoretical Normalized Relative Jones Tensor Elements for z-Cut Quartz Oriented at 0°

	theoretical	experimental (magnitude)
χ_{nhh}	−0.58	0.52 ± 0.06
χ_{nvh}	−0.58	0.61 ± 0.03
χ_{nvv}	0.58	0.59 ± 0.03

Evaluation of the measurement approach was next assessed in polarization-modulated measurements of naproxen crystals, summarized in Figures 5 and 6. Figure 5a corresponds to overall intensity of the horizontally polarized SHG channel, generated by integrating the 10 unique polarization-dependent images. Figure 5b corresponds to those same results separated out into the 10 unique polarization states sampled at each pixel during different time-points in the EOM cycle. Figure 5c

contains images of the Fourier coefficient values recovered by linear fitting of the 10 images in Figure 5b to eq 5. These Fourier coefficient images represent the full native information content available from the measurements. To concisely represent these images, the five coefficient images were mapped onto a five color scheme: red, greed, blue cyan and magenta (RGBCM). The intensity of Fourier coefficient a was displayed on a scale of 0−40 mV, and coefficients $b−e$ were displayed on a scale of 0−20 mV. The relative amplitudes of the native coefficients could then be recovered simply by separation into the individual color elements.

A complete set of results for naproxen for all three detectors is summarized in Figure 6, with panels (a)−(c) representing integrated intensity for the horizontal PMT, vertical PMT, and laser transmittance, respectively. Figure 6d and e corresponds to the coefficient color maps as determined from the linear fitting
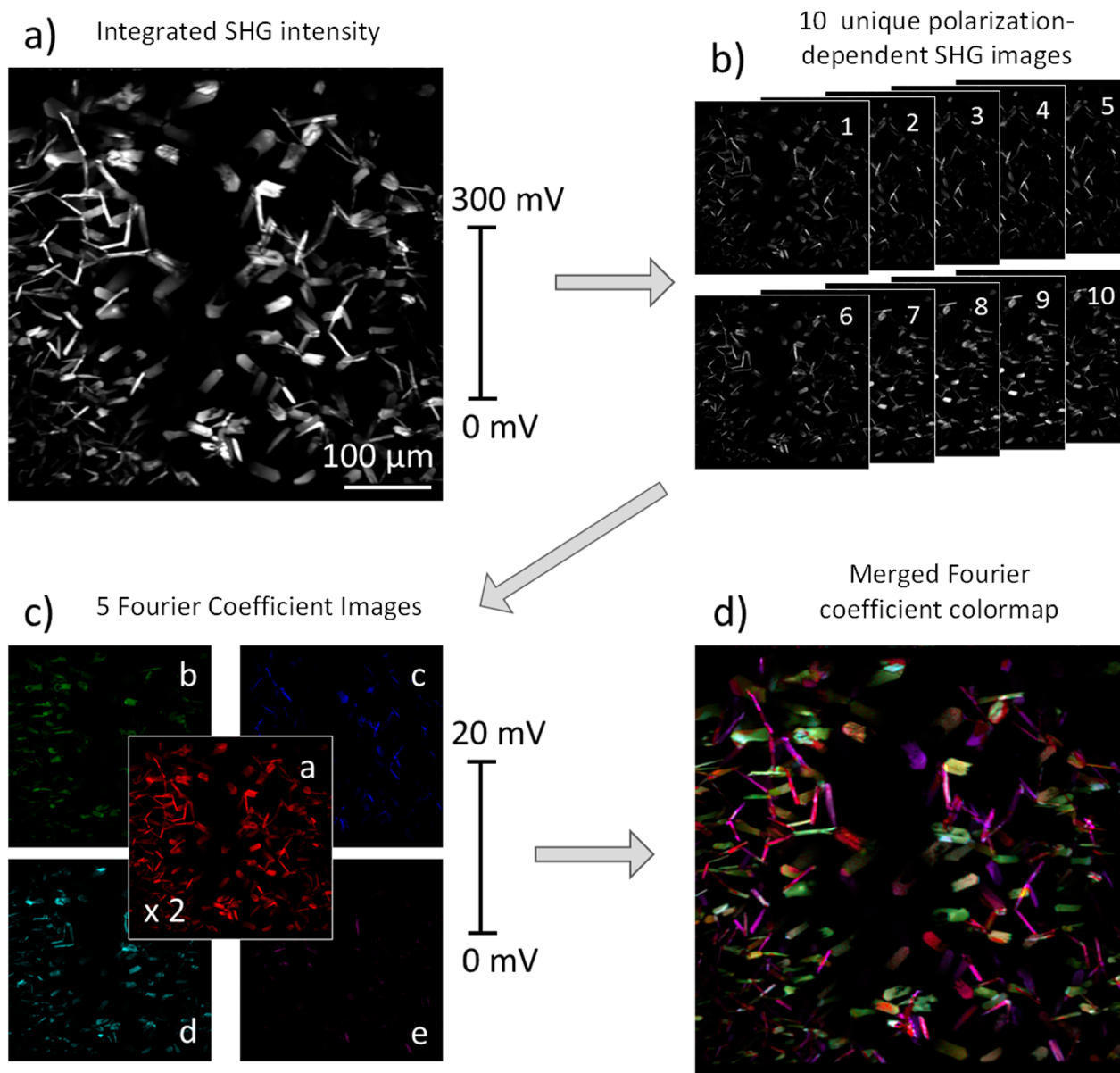

Figure 5. Summary of polarization-modulation SHG results for naproxen crystals for the horizontal PMT. An overall intensity image (a) and the same image separated out into its 10 unique polarization-dependent images (b) are shown. The five Fourier coefficient images are shown in (c), with each coefficient representing a unique color (red, green, blue, cyan and magenta for coefficients a, b, c, d, and e, respectively). The five coefficient images were then merged into a single five-color image, shown in (d).
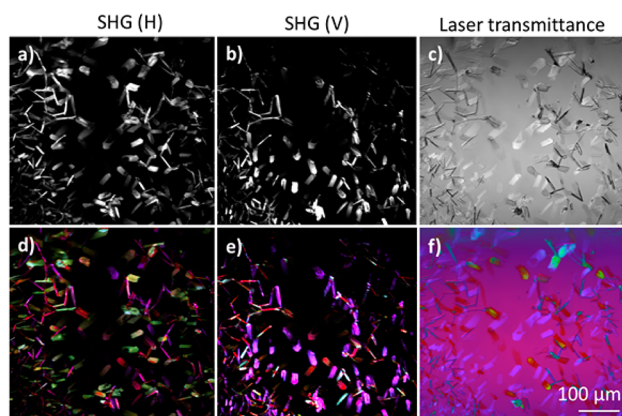
Figure 6. Integrated intensity images of index matched naproxen crystals for (a) horizontally polarized SHG, (b) vertically polarized SHG, and (c) polarized laser transmittance, with corresponding Fourier coefficient color maps in (d)−(f).

to eq 5. for SHG (shown on the same color scale as Figure 5) and Figure 6f shows the coefficient color map image as determined form the linear fitting to eq 7 for laser transmittance. Figure 6f is composed of Fourier coefficients *a*, *b*, and *c*, represented by the colors red, green and blue, respectively. In order to display all three coefficients on the same image, coefficient a (red) was displayed on a scale of 0 to +0.3 V, coefficient b (green) was displayed on a scale of −0.3 to 0.0 V and coefficient c was displayed on a scale of −0.15 to +0.15 V. A representative result of the linear fitting for laser transmittance of a single pixel from a naproxen crystal is shown in Figure S-3 in the Supporting Information. The images in Figures 5 and 6 were produced using signal averaging for improved quality, but the analysis can be performed on images acquired with continuous sampling at video rate. A video frame of the color-encoded polarization maps for naproxen crystals obtained at 15 Hz frame rates is shown in Figure 7. The naproxen crystals shown in the
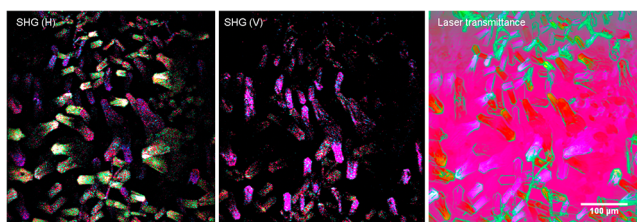

Figure 7. Video frame of color encoded Fourier coefficient color maps for naproxen crystals being translated in the *X/Y* plane (also see the video). Polarization data were acquired in real time simultaneously on all three channels (horizontal-SHG, vertical-SHG, and laser transmittance). The sample was translated using an automated prior-stage during imaging.

video were not index matched in oil, making edge effects more pronounced in the laser transmittance color maps when compared to the crystals in Figure 6f.

Additional measurements were performed for a multidomain protein crystal, shown in Figure 8. Polarization-dependent images were acquired at 11 z-slices through the aqueous drop to generate a 3D polarization color map of the crystal. Figure 8a corresponds to a laser transmittance image integrated over all 10 polarizations for a single z-slice, suggesting two crystalline domains based on crystal habit. Figure 8b shows a 3D image obtained by performing principal component analysis (PCA) of
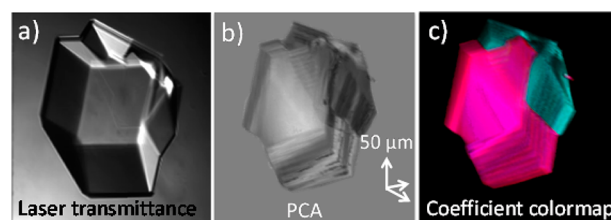

Figure 8. Images of a multidomain glucose isomerase crystal. A 2D laser transmittance image of a multidomain glucose isomerase crystal integrated for all 10 polarizations is shown in (a). Corresponding 3D PCA (principal component 2) and Fourier coefficient false color images are shown for the horizontal SHG detector in (b) and (c), respectively.

the pooled set of 10 different polarization-dependent images for each z-slice. Previously, multidomain crystals have been identified using PCA of polarization-dependent SHG images as an assessment of crystal diffraction quality based on training using measurements obtained over a large number of similar protein crystals.[13] In comparison, Figure 8c shows a 3D Fourier coefficient color map obtained through NOSE analysis of the 10 polarization dependent images acquired for each z-slice without the need for training. The coefficient images of glucose isomerase were treated in the same manner as the naproxen sample with respect to the scaling of the coefficients.

In this particular case, NOSE analysis provided significantly higher contrast for visualization of protein crystal domains compared to the same polarization-dependent images analyzed with PCA. NOSE has the additional distinct advantage of requiring no training prior to domain discrimination. In addition, drift in the EOM response between samples, or from measurements acquired on different days or on different instruments typically alter the principal axes, such that PCA requires routine retraining. In contrast, NOSE analysis acquired on a calibrated instrument should be consistent, even with different EOM settings or in the presence of measured drift.

It is interesting to compare the NOSE microscope figures of merit to those of previous single-point nonlinear optical ellipsometry instruments.[18,21,24,25,28,29] At video rate, pixels in the central field of view are sampled with as few as 12 consecutive laser pulses, each of which corresponds to one of the 10 possible polarization states produced by the EOM. The value of 12 laser pulses represents a minimum, with a greater number of pulses sampled per pixel near the edges of the fast scan axis where the resonant mirror was moving the beam more slowly. Compared to the 12.5 ms acquisition time used previously, the minimum per-pixel acquisition time for z-cut was 4.8 μs (32 averaged frames, each 150 ns), representing a 2600-fold reduction in the measurement time. Assuming noise is dominated by Poisson fluctuations in the detected intensity, this change corresponds to an anticipated reduction of ∼50 in the signal-to-noise ratio (SNR) relative to the previous polarization measurements by NOSE. In that prior work, quartz tensor elements could be determined in 12.5 ms with a SNR of ∼100. Reducing this value by a factor of 50 yields a SNR ratio of approximately 2 in 4.8 μs. In practice, the measured SNR in a single pixel in an integration time of 4.8 μs in the current NOSE experiments was typically approximately 5−6, representing approximately a 3-fold increase over previous experiments. The most likely explanation for the improvement in the SNR in the present work is the higher signal level achievable using fast scanning and synchronous digitization for high dynamic range

detection rather than photon counting as was done in the previous work.

Because the data were initially fit to a set of Fourier coefficients, it may be tempting to suggest that high speed lock-in amplification (LIA) could serve as an alternative platform for recovery of the coefficients. However, the expressions in eq 5 and eq 7 represent a Fourier series in the EOM phase shift, Δ, not in time. While $\Delta(t)$ is sinusoidally modulated in time, the intensity of the SHG given by eq 5 depends nontrivially on trigonometric functions of the sinusoidal function $\Delta(t)$. It is only in the limit of low amplitude modulation that $\Delta(t) \cong A(2\pi f_0 t + \delta) + B$, such that the harmonics in time correspond to the harmonics in Δ. Lowering the modulation amplitude to maintain this approximate relationship restricts one to relatively shallow depths of polarization modulation, which in turn reduces the confidence in the recovered coefficients. From a practical standpoint, most LIAs operate at a single frequency, such that two LIAs would be needed for each detector to access the full set of coefficients expressed in eq 5. Maintaining careful calibration between the amplitudes of each LIA together with the zero-frequency DC response is nontrivial. In addition, the central advantages of LIA in terms of bandwidth reduction and phase-sensitive detection become less pronounced as the acquisition times are reduced. The detection bandwidth scales inversely with the sampling time, which for a minimum of a 125 ns acquisition time corresponds to 32 MHz of frequency bandwidth about the center frequency in the underlying electronics. Interestingly, the LIA's now commercially available to achieve detection at MHz modulation frequencies are based on high-speed digitization qualitatively similar to the oscilloscope cards used in the present study, but without the advantages of SD[15,19] and user-defined data analysis.

As can be seen from the coefficient color map images in Figures 5 and 6, the polarization-dependence of SHG varies significantly for different naproxen crystals depending on their orientation relative to the image axes. The variation in polarization-dependence is attributed largely to the differences in crystal orientation relative to the laboratory frame. The overall similarity of the color-map hues for different crystals at similar rotation angles is consistent with this explanation. Indeed, such good agreement between similarly azimuthally oriented crystals is somewhat surprising, given that the azimuthal rotation angle is just one of the three possible rotation angles available to the crystals. Additional variability in the tilt angle into/out of the focal plane and the twist angle would generally be expected to introduce greater diversity in the polarization-dependent responses. This absence of diversity is tentatively attributed to nonisotropic orientation distributions due to templating by the glass interface. Heterogeneous nucleation is quite common, driven by the lower free energy barrier introduced for clusters at the interface relative to within the bulk. Furthermore, the interfacial energy at the crystal/glass interface will be dependent on the particular crystal plane positioned at the interface, such that thermodynamics will favor a particular tilt and twist angle relative to the interface. Under these conditions, only the azimuthal rotation angle is fully unconstrained.

This reduction in orientational diversity for materials crystallized on a glass surface is highly advantageous, as it reduces a potentially complicated relationship between the crystal orientation and the laboratory frame response. If only azimuthal orientation is unique from crystal to crystal, the analysis is reduced down to a relatively simple one, based on

relations similar to those described in the Supporting Information for treating the rotated z-cut quartz. Provided the crystal azimuthal rotation angle is determined independently in advance (e.g., from image analysis), NOSE should enable recovery of the crystal tensor in the crystal frame from the Jones tensor elements measured in the laboratory frame. In this manner, NOSE may potentially serve as a reliable orientation-independent identifier for crystal polymorphism in APIs.

Both the naproxen crystals and the two crystalline domains of glucose isomerase exhibited large variations in polarization response as a function of crystallographic orientation. It is also of note that the net polarization response of naproxen appears to differ from the net polarization response of glucose isomerase. For the horizontal SHG channel, the naproxen color-map contains largely red, green, and purple, whereas the glucose isomerase 3D color map contains crystalline domains of cyan and magenta. This difference between samples suggests not only the ability to distinguish between differently oriented crystals, but also between different types of crystalline materials. This shows promise in the area of API polymorph screening, in cases where full orientation mapping and therefore full NOSE analysis is not possible.

The sensitivity to crystal orientation may also potentially be beneficial in the identification of crystal twinning prior to structure determination. Twinning is a similar phenomenon to the case of multidomain crystal formation, as shown for glucose isomerase in Figure 8, but is often impossible to identify with conventional optical imaging, especially in the case of merohedral twinning.[30] Twinning can significantly complicate structure determination from X-ray diffraction, yet a rapid, nondestructive and sensitive screening method for twinning is still lacking. The differences in the polarization-dependent NLO properties of differently oriented twin domains may in principle provide contrast for the identification of twinned crystals.

A key long-term goal of this measurement platform is the recovery of the local-frame tensor to assess subtle changes in local structure from the polarization-dependence of SHG, analogous to the measurements performed for z-cut quartz. For crystals, the polarization-dependence could be used to sensitively detect changes in crystal polymorphism for high-throughput API crystal screening applications. In studies of collagen, subtle local structural changes within the fibers can serve as indicators for different collagen types. In these applications, the laboratory frame Jones tensor elements depend on the sample orientation within the field of view, on the nonlinear optical properties of the samples, and on the linear properties through sample birefringence. In z-cut quartz, the absolute orientation of the sample was known a priori and the sample exhibits no birefringence, considerably simplifying the analysis. Disentangling the roles of each of these additional effects using model-dependent analyses of the model-independent measurements represents an effort beyond the scope of the present study. However, the simultaneous acquisition of both the polarization-dependent SHG together with the polarized laser transmittance from that same location will help inform such analyses. Those efforts are currently in progress and will likely be the subject of subsequent publications.

■ CONCLUSIONS

The theoretical framework for SHG ellipsometric microscopy has been presented and experimentally verified. By incorporating fast polarization modulation with SD, it has been shown to

provide a substantial reduction in acquisition time as compared to previous NOSE techniques without significant loss in precision, allowing for real-time imaging applications. Validation of the technique and instrumentation was performed using z-cut quartz with well characterized NLO properties as a reference. The experimentally measured Jones tensor elements for z-cut quartz fell within error of the theoretical predicted values. The technique was further used to explore naproxen and glucose isomerase crystals with the resulting Fourier coefficient images showing substantial differences due to crystal orientation. Furthermore, the Fourier coefficient maps of naproxen as compared to glucose isomerase crystals demonstrate an overall net coefficient difference, potentially allowing for not only differentiation of crystal orientation but also discrimination of different crystalline material. Lastly, it was demonstrated that by coupling fast polarization modulation synchronously with detection, the signal-to-noise of the measurement was sufficient to perform real-time (15 Hz) polarization-dependent imaging with as little as 150 ns per pixel integration time and still recover statistically significant Fourier coefficients directly connected to the tensors defining linear and nonlinear optical properties of the sample.

ASSOCIATED CONTENT

Ⓢ Supporting Information

Mathematical methods used to recover the local-frame $\chi^{(2)}$ tensor elements for quartz from the laboratory-frame measurements of the Jones tensor for the rotated quartz are given. Information describing details regarding the data acquisition for image construction with nonuniform sampling from the sinusoidal resonant mirror trace is shown. In addition, independent plots of all five Fourier coefficients for z-cut quartz are shown (only two are shown in Figure 4 of the main article). Representative linear fit is also shown for recovery of the birefringence coefficient images in Figures 6 and 7, as well as analytical expressions for recovering parameters related to birefringence from the transmitted fundamental beam. A video displaying the 30 polarization-dependent images obtained in a single measurement of naproxen crystals is available. This material is available free of charge via the Internet at http://pubs.acs.org/.

Ⓦ Web-Enhanced Feature

A video of the color-encoded polarization maps of naproxen crystals obtained at video rate is available in the HTML version of the paper.

AUTHOR INFORMATION

Corresponding Author
*E-mail: gsimpson@purdue.edu.
Notes
The authors declare no competing financial interest.

ACKNOWLEDGMENTS

REFERENCES

(1) Campagnola, P. J.; Millard, A. C.; Terasaki, M.; Hoppe, P. E.; Malone, C. J.; Mohler, W. A. *Biophys. J.* **2002**, *81*, 493.
(2) Stoller, P.; Reiser, K. M.; Celliers, P. M.; Rubenchik, A. M. *Biophys. J.* **2002**, *82*, 3330.
(3) Gusachenko, I.; Tran, V.; Houssen, Y. G.; Allain, J. M.; Schanne-Klein, M. C. *Biophys. J.* **2012**, *102*, 2220.
(4) Moreaux, L.; Sandre, O.; Mertz, J. *J. Opt. Soc. Am. B* **2000**, *17*, 1685.
(5) Plotnikov, S.; Millard, A. C.; Campagnola, P. J.; Mohler, M. *Biophys. J.* **2006**, *90*, 693.
(6) Brasselet, S. *Adv. Opt. Photonics* **2011**, *3*, 205.
(7) Lin, S. J.; Jee, S. H.; Kuo, C. J.; Wu, R. J.; Lin, W. C.; Chen, J. S.; Liao, Y. H.; Hsu, C. J.; Tsai, T. F.; Chen, Y. F.; Dong, C. Y. *Opt. Lett.* **2006**, *31*, 2756.
(8) Le, T. T.; Langohr, I. M.; Locker, M. J.; Sturek, M.; Cheng, J. X. *J. Biomed Opt.* **2007**, *12*, 054007.
(9) Latour, G.; Gusachenko, I.; Kowalczuk, L.; Lamarre, I.; Schanne-Klein, M. *Biomed. Opt. Express* **2012**, *3*, 1.
(10) Brasselet, S.; Zyss, J. *C. R. Phys.* **2007**, *8*, 165.
(11) Sandeau, N.; Le Xuan, L.; Chauvat, D.; Zhou, C.; Roch, J. F.; Brasselet, S. *Opt. Express* **2007**, *15*, 16051.
(12) Chowdhury, A. U.; Dettmar, C. M.; Sullivan, Z. S.; Zhang, S.; Harden, S. E.; Jacobs, K. T.; Ingram, N.; Kissick, D. J.; Wanapun, D.; Maltais, T.; Simpson, G. J. *J. Am. Chem. Soc.* **2014**, *136*, 2404.
(13) DeWalt, E. L.; Begue, V. J.; Ronau, J. A.; Sullivan, S. Z.; Das, C.; Simpson, G. J. *Acta Crystallogr., Sect. D* **2013**, *69*, 74.
(14) Begue, N. J.; Simpson, G. J. *Anal. Chem.* **2010**, *82*, 559.
(15) Anceau, C.; Brasselet, S.; Zyss, J. *Chem. Phys. Lett.* **2005**, *411*, 98.
(16) Tanaka, Y.; Hase, E.; Fukushima, S.; Ogura, Y.; Yamashita, T.; Hirao, T.; Araki, T.; Yasui, T. *Biomed. Opt. Express* **2014**, *5*, 1099.
(17) Lien, C.-H.; Tilbury, K.; Chen, S.-J.; Campagnola, P. J. *Biomed. Opt. Express* **2013**, *4*, 1991.
(18) Begue, N. J.; Moad, A. J.; Simpson, G. J. *J. Phys. Chem. C* **2009**, *113*, 10158.
(19) Kissick, D. J.; Muir, R. D.; Sullivan, S. Z.; Oglesbee, R. A.; Simpson, G. J. *Proc. SPIE* **2013**, *8657*, 86570E.
(20) Muir, R. D.; Sullivan, S. Z.; Oglesbee, R. A.; Simpson, G. J. *Rev. Sci. Instrum.* **2014**, *85*, 033703.
(21) Polizzi, M. A.; Plocinik, R. M.; Simpson, G. J. *J. Am. Chem. Soc.* **2005**, *127*, 1058.
(22) Dettmar, C. M.; Simpson, G. J. In *Second Harmonic Generation Imaging*; Pavone, F. S., Campagnola, P. J., Eds.; CRC Press: Boca Raton, FL, 2013; p 3.
(23) Azzam, R. M. A.; Bashara, N. M. *Ellipsometry and Polarized Light*; Elsevier: Amsterdam, 1987.
(24) Begue, N. J.; Everly, R. M.; Hall, V. J.; Haupert, L.; Simpson, G. J. *J. Phys. Chem. C* **2009**, *113*, 10166.
(25) Plocinik, R. M.; Everly, R. M.; Moad, A. J.; Simpson, G. J. *Phys. Rev. B* **2005**, *72*, 125409.
(26) Robinson, P. B. D. K. *Data Reduction and Error Analysis for the Physical Sciences*; 3rd ed.; McGraw-Hill: New York, 2002.
(27) Boyd, R. W. *Nonlinear Optics*, 2nd ed.; Academic Press: Amsterdam, 2003.
(28) Plocinik, R. M.; Simpson, G. J. *Anal. Chim. Acta* **2003**, *496*, 133.
(29) Dehen, C. J.; Everly, R. M.; Plocinik, R.; Simpson, G. J. *Rev. Sci. Instrum.* **2007**, *78*, 013106.
(30) Yeates, T. O.; Fam, B. C. *Structure* **1999**, *7*, R25.